

Mixture-of-Experts Transformer for Automatic Modulation Recognition

Jiale Wang, Wupeng Xie, Yaxin Mu, Xin Liu, Zhilong Zhao, and Jingwei Zhang

Abstract—Automatic Modulation Recognition (AMR) is a key enabling technology for cognitive radio and intelligent spectrum management in next-generation wireless systems. However, current deep learning-based AMR methods predominantly rely on static multi-scale fusion strategies, which lack the flexibility to adapt to the highly dynamic temporal variations of modulation signals. To address this limitation, we propose MoEformer, an adaptive Multi-Scale Mixture-of-Experts Transformer network that directly processes I/Q signals to preserve their temporal and phase structures. Specifically, MoEformer constructs multi-scale expert views through temporal resampling, employs an input-dependent gating mechanism for dynamic expert fusion, and integrates Rotary Position Embeddings (RoPE) within Transformer encoders to capture both local and global temporal dependencies. Comprehensive evaluations on three widely adopted benchmarks (RadioML2016.10a, RadioML2016.10b, and RadioML2018.01A) demonstrate that MoEformer outperforms the competitive baselines, achieving superior average recognition accuracies of 63.74%, 66.24%, and 64.22%, respectively. In addition, the proposed method strikes an optimal trade-off between recognition performance and model complexity.

Index Terms—Automatic modulation recognition, mixture-of-experts, deep learning, transformer.

I. INTRODUCTION

THE explosive proliferation of Internet-of-Things (IoT) devices and heterogeneous wireless services has made intelligent spectrum awareness a fundamental requirement for future wireless systems. Cognitive Radio (CR) has been widely recognized as a promising paradigm for improving spectral efficiency through dynamic spectrum access [1]. In this context, Automatic Modulation Recognition (AMR), as a key physical-layer technology, aims to identify the modulation format of a received signal in non-cooperative scenarios without requiring prior knowledge of the transmitter or channel state information [2]. This capability is indispensable in a broad range of applications, including cognitive radio, dynamic spectrum access, interference monitoring, anomaly detection, electronic warfare, and communication surveillance [3]. More broadly, as wireless networks evolve toward increasingly autonomous and adaptive architectures, AMR is becoming a core enabling component for intelligent signal perception,

spectrum management, and resource allocation [4]. In resource-constrained and dynamic environments, efficient and robust AMR becomes particularly critical.

Early studies on AMR mainly followed two classical lines of research, namely likelihood-based (LB) and feature-based (FB) methods [5]. Likelihood-based approaches derive classification decisions through statistical hypothesis testing and can achieve strong theoretical optimality under ideal assumptions [6]. However, their applicability in practice is severely limited by prohibitive computational complexity and the need for accurate prior knowledge of channel parameters, noise statistics, and signal models. Feature-based methods alleviate these issues by extracting handcrafted descriptors, such as instantaneous statistics [7], spectral features [8], and higher-order cumulants [9], and then feeding them into conventional classifiers such as decision trees or Support Vector Machines (SVMs) [10]. Although more computationally tractable, such methods remain fundamentally constrained by the quality and generality of manually designed features. Their performance often deteriorates substantially in low-SNR regimes, under fading and synchronization impairments, or when the signal environment deviates from the assumptions embedded in the feature design [11].

The rise of deep learning has fundamentally shifted AMR toward end-to-end representation learning, bypassing the need for handcrafted features. Pioneering work by O’Shea *et al.* demonstrated that convolutional neural networks (CNNs) can extract discriminative patterns directly from raw in-phase and quadrature (I/Q) sequences, establishing deep learning as a mainstream paradigm [12]–[14]. CNN-based models exploit local receptive fields and weight sharing to learn hierarchical local patterns from received signals, and have shown strong performance on widely used benchmarks [15], [16]. To address degradation issues in deeper networks, O’Shea *et al.* further introduced residual connections into AMR models and showed that ResNet-style architectures can achieve superior recognition performance, especially under high SNR conditions [17], [18]. To further leverage mature computer vision backbones, subsequent research sought to transform these 1D temporal signals into 2D image-like representations [19]. For example, Peng mapped received signals into constellation diagrams and employed AlexNet [20] and GoogLeNet [21] to capture clustering patterns, which proved particularly effective for discriminating QAM signals [22]. Other studies used short-time Fourier transform (STFT) [23] or wavelet transform [24] to generate time–frequency representations and then reformulated AMR as an image classification problem. While such approaches can incorporate useful prior knowledge from the transform domain and sometimes improve feature separability, they generally introduce additional computational cost and may incur information loss during signal transformation. More

Jiale Wang and Yaxin Mu are with the Beijing Information Science and Technology University, Beijing 100101, China (e-mail: jiale.wang@bistu.edu.cn; yaxinmu@bistu.edu.cn).

Wupeng Xie is with the Intelligent Technology Research Institute of China Electronics Technology Group Corporation, Beijing 100041, China (e-mail: wupengxie@cetc.com.cn).

Xin Liu is with the Beijing Institute of Satellite Information Engineering, Beijing 100095, China (e-mail: liuxin115@mails.ucas.ac.cn).

Zhilong Zhao is with the University of Chinese Academy of Sciences, Beijing 100049, China (e-mail: zhaozhilong09@mails.ucas.ac.cn).

Jingwei Zhang is with the School of Electronics Engineering, Aerospace Information Technology University, Jinan, Shandong, China (e-mail: zhangjingwei14@mails.ucas.edu.cn).

Corresponding author: Wupeng Xie.

importantly, standard CNNs still rely on static receptive fields, which limits their ability to capture long-range temporal dependencies inherent in modulation signals [25].

To address the sequence-modeling bottlenecks of CNNs, early efforts turned to recurrent neural networks (RNNs) to explicitly capture temporal dynamics. Studies utilizing variants such as LSTMs [26] and GRUs [27] demonstrated that recurrent architectures can effectively model sequential dependencies in radio signals [28]. However, RNN-based approaches generally suffer from limited parallelism, low computational efficiency, and slow convergence especially over long observation windows. Inspired by their remarkable success in natural language processing [29], speech recognition [30], and computer vision [31], Transformer architectures [32] have recently emerged as a powerful alternative to recurrent models in the AMR domain [33]–[35]. This growing interest is primarily driven by their self-attention mechanism, which facilitates highly parallelized modeling of long-range dependencies. For instance, Hamidi-Rad *et al.* proposed MCformer [36], which successfully couples a convolutional front-end with Transformer blocks, achieving robust global feature extraction with relatively low parameter complexity. Nevertheless, these models [37] typically employ invariant fusion strategies that lack input-adaptivity. Such fixed integration fails to account for the signal-specific temporal nuances inherent in heterogeneous wireless environments.

Fundamentally, AMR constitutes a multi-scale temporal inference problem complicated by non-stationary channel impairments. Discriminative features span instantaneous phase transitions, short-term envelope fluctuations, and long-range temporal evolutions induced by pulse shaping, carrier frequency offsets (CFO), and multi-path fading [37]. These heterogeneous structures vary across modulation formats as well as channel and SNR conditions, making static fusion strategies suboptimal. Although CNNs can effectively capture local features, their receptive fields remain largely fixed. Even when multiple branches or kernels are employed, the resulting fusion is typically static, implicitly assuming that the importance of each temporal scale is constant across samples. A standard Transformer, while powerful for modeling long-range dependencies, does not inherently solve the scale-selection problem. This limitation becomes even more pronounced under realistic AMR conditions, where low SNR and high inter-class similarity often obscure modulation-specific structures [38]. In such scenarios, an effective AMR model must not only capture long-range dependencies, but also adaptively emphasize the most informative temporal patterns while suppressing noisy or irrelevant content. To resolve this tension between representational flexibility and computational efficiency, we leverage the Mixture-of-Experts (MoE) paradigm to construct an input-adaptive framework [39]–[42]. MoE mechanism allows different experts to specialize in different temporal resolutions or structural patterns, while a routing module adaptively determines how strongly each expert should contribute. This dynamic routing explicitly aligns with the physical characteristics of AMR. Specifically, it allocates high-resolution experts to capture rapid symbol transitions, while routing slow phase and envelope variations to experts with wider receptive fields. Consequently, MoE provides a deterministic mechanism to resolve the temporal heterogeneity

of modulation signals in non-cooperative environments.

Motivated by these considerations, we propose MoEformer, a Multi-Scale Mixture-of-Experts Transformer network that operates directly on raw I/Q sequences to preserve native temporal structures. To capture diverse modulation patterns, the model employs time-scaling resampling to generate multi-resolution views for scale-specific experts. Unlike static multi-branch architectures, MoEformer introduces an input-dependent gating mechanism that adaptively weights these experts based on the global characteristics of each signal sample. For coherent integration, frequency-domain resampling aligns the heterogeneous representations to a unified length, ensuring spectral consistency during cross-scale fusion. The resulting features are then processed by a Transformer encoder integrated with Rotary Position Embedding (RoPE) [43], which provides a relative-position inductive bias tailored to wireless signal dynamics. ly, an attention pooling mechanism aggregates temporal features to preserve discriminative signal segments that would otherwise be diluted by uniform averaging.

In summary, the proposed framework focuses on effectively integrating discriminative features across multiple temporal scales while maintaining robustness against noise and channel impairments. By incorporating input-adaptive multi-scale routing, cross-scale feature alignment, and attention-based temporal aggregation into a unified end-to-end architecture, MoEformer provides a flexible and efficient solution for automatic modulation recognition.

The main contributions of this work are summarized as follows:

- 1) We develop a signal-consistent multi-scale representation framework in which temporal resampling enables scale-specialized experts to capture resolution-dependent modulation patterns. Frequency-domain resampling aligns multi-scale features to a unified length while preserving spectral consistency
- 2) We introduce an adaptive expert weighting mechanism via gating networks, enabling dynamic allocation of representational capacity across temporal scales. Compared with static multi-scale fusion, this strategy enhances scale-specific specialization while mitigating redundant feature aggregation.
- 3) We provide a signal-consistent interpretation of RoPE for AMR, showing that its rotation-based encoding aligns naturally with the phase evolution of complex modulation signals. Combined with attention-based pooling, this design improves robustness to temporal misalignment and noise.
- 4) Extensive experiments on three benchmark datasets (RadioML2016.10a/b and RadioML2018.01A) demonstrate that MoEformer achieves highly competitive performance using only raw I/Q inputs, without relying on handcrafted features or time–frequency transformations, while maintaining improved parameter efficiency.

II. PROBLEM FORMULATION

A. Signal Model

Consider a wireless communication system in which the transmitter selects a modulation scheme from a predefined

set $\mathcal{M} = \{M_1, \dots, M_K\}$ and generates a complex baseband signal $s(t)$. The received signal at a non-cooperative receiver is subject to multipath fading, carrier frequency offset (CFO), phase offset, and additive noise, and can be mathematically modeled as

$$r(t) = (h(t) * s(t))e^{j(2\pi\Delta f t + \theta)} + n(t), \quad (1)$$

where $h(t)$ denotes the channel impulse response, $*$ denotes the linear convolution operation, Δf represents the normalized CFO, θ is a phase offset, and $n(t)$ represents complex additive white Gaussian noise (AWGN) with zero mean and variance σ^2 . The received signal is uniformly sampled to obtain a discrete-time sequence $r[n]$, which is decomposed into in-phase (I) and quadrature (Q) components. The input to the neural network is constructed as a real-valued matrix

$$\mathbf{X} = \begin{bmatrix} r_I[0] & r_I[1] & \cdots & r_I[N-1] \\ r_Q[0] & r_Q[1] & \cdots & r_Q[N-1] \end{bmatrix}, \quad (2)$$

where $r_I[n]$ and $r_Q[n]$ denote the in-phase and quadrature components of the sampled received signal $r[n]$.

B. Multi-Scale Temporal Nature of Modulation Signals

Before formulating the classification objective, it is essential to analyze the intrinsic multi-scale nature of modulation signals. This underlying physical property fundamentally dictates the architectural requirements for an effective recognition system.

Modulation recognition is essentially a temporal inference problem under stochastic channel distortions. Modulation signals encode information through instantaneous symbol transitions, multi-symbol memory effects, and long-range phase evolution. Crucially, these temporal structures manifest across multiple resolutions, with their discriminative contributions varying significantly depending on the modulation scheme and channel conditions.

Within individual symbol intervals, digital modulations encode information through instantaneous phase transitions and amplitude variations. These short-term dynamics provide primary discriminative cues, although their reliability degrades progressively under severe noise. Beyond individual symbols, pulse shaping and inter-symbol interference introduce multi-symbol dependencies that shape the signal envelope and constellation dynamics, contributing essential information for distinguishing modulation families. Over longer timescales, channel impairments such as carrier frequency offset and slow fading induce gradual phase rotation and envelope drift, where discriminative information lies in relative phase evolution rather than instantaneous transitions.

The relative dominance of these scales varies dynamically across inputs: high-SNR digital modulations are predominantly characterized by symbol-level structure, while low-SNR or analog modulations rely more heavily on long-range temporal characteristics. This input-dependent variability highlights a critical mismatch in feature extractors that operate at a fixed temporal resolution, which implicitly apply uniform representational capacity across all scales. Consequently, this behavior motivates the necessity for an adaptive multi-scale mechanism capable of dynamically allocating network capacity according to the global characteristics of each input signal.

C. Learning Objective and Motivation

Modulation recognition can be mathematically formulated as a K -class classification problem. Given an observed I/Q sequence \mathbf{X} , the primary objective is to learn a mapping function $f_\theta(\cdot)$ parameterized by θ such that

$$\hat{y} = \arg \max_{M_k \in \mathcal{M}} P(M_k | \mathbf{X}; \theta). \quad (3)$$

A fundamental challenge lies in dynamically integrating discriminative features across heterogeneous temporal scales while remaining robust to channel-induced distortions. As demonstrated by the preceding analysis of signal dynamics, the dominant temporal structure varies significantly across modulation schemes and channel conditions. Nevertheless, existing deep learning approaches impose rigid structural constraints that prevent effective adaptation to this inherent variability.

While existing deep learning architectures have achieved empirical success in AMR, addressing the objective above requires two specific structural capabilities. First, it requires dynamic weight allocation rather than static receptive fields, as the relative importance of different temporal resolutions is not constant but highly input-dependent. Second, it requires physically meaningful relative temporal modeling—such as capturing the relative phase rotation induced by CFO—which is often suboptimal when relying on absolute positional encodings.

Taken together, these requirements indicate that bridging the gap between complex signal dynamics and accurate classification necessitates an input-adaptive multi-scale inference mechanism coupled with relative positional modeling. This core motivation directly drives the architectural design of our proposed MoEformer, which leverages a Mixture-of-Experts framework with dynamic gating and Rotary Position Embeddings to meet these objectives, as detailed in Section III.

III. METHOD

As illustrated in Fig. 1, we propose MoEformer, an adaptive multi-scale mixture-of-experts architecture designed to dynamically allocate representational capacity across heterogeneous signal scales. The proposed framework operates in three sequential stages. First, a multi-scale MoE front-end extracts and adaptively fuses scale-specific local features. Second, a series of Transformer encoders with relative positional awareness models global temporal dependencies. Finally, an attention pooling mechanism aggregates salient temporal cues into a unified global representation, which is then processed by a classifier to yield the final prediction.

A. MoE Feature Extractor

1) *Time-Domain Resampling*: Let $\mathbf{X} \in \mathbb{R}^{B \times 2 \times L}$ denote a normalized input I/Q sequence, with batch size B and sequence length L . To capture heterogeneous temporal features, we route the sequence through N independent experts. Based on a predefined set of scale factors $\{s_i\}_{i=1}^N$, the input for the i -th expert is dynamically resampled as:

$$\mathbf{X}_i = \mathcal{T}_{s_i}(\mathbf{X}) \in \mathbb{R}^{B \times 2 \times L_i}, \quad L_i = \lfloor s_i L \rfloor \quad (4)$$

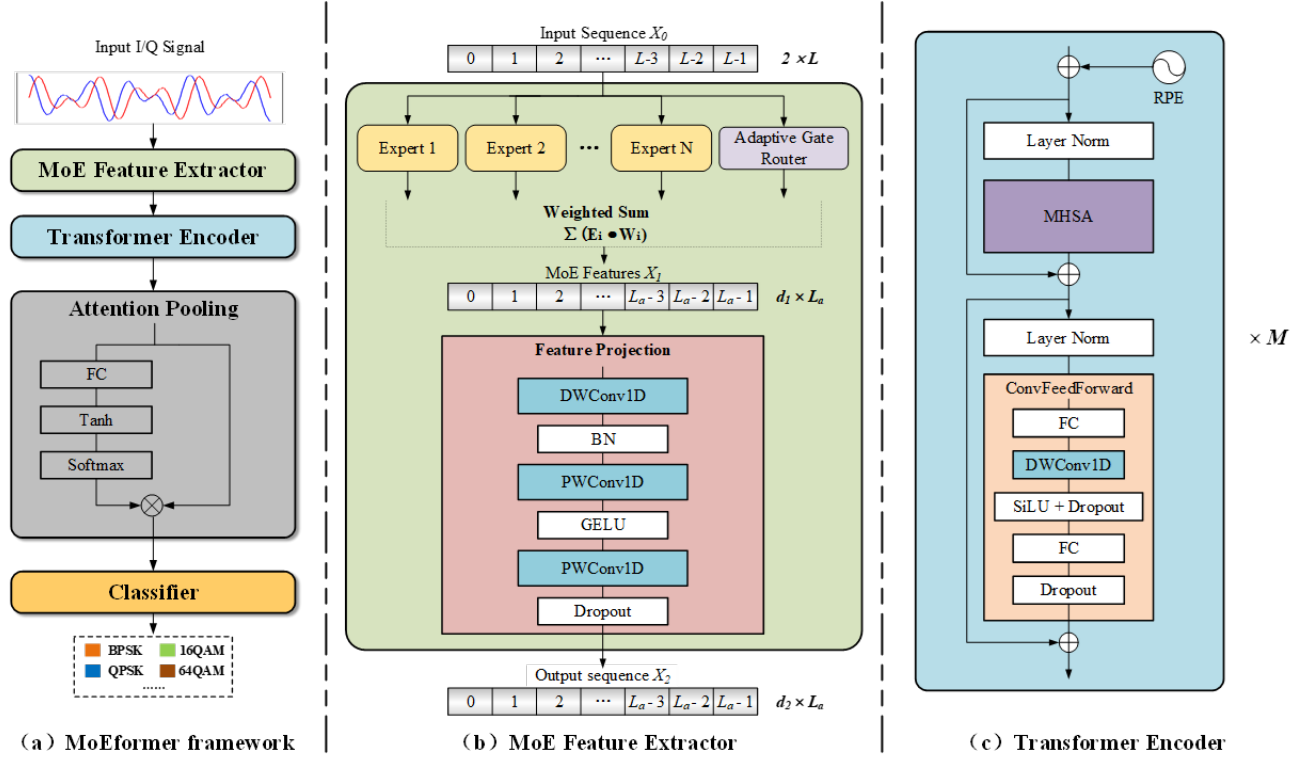


Fig. 1. Overall architecture of the proposed MoEformer.

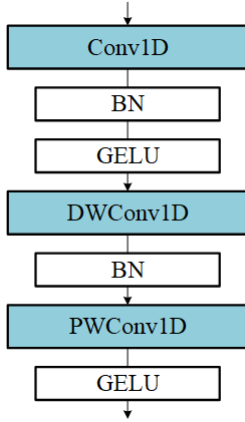


Fig. 2. Architecture of the Local Representation Block (LRB).

where $\mathcal{T}_{s_i}(\cdot)$ denotes linear interpolation. Instead of adjusting convolutional kernel sizes, we modulate the temporal resolution of input features to drive each expert to specialize in unique temporal scales.

Each resampled view is then processed by a dedicated expert module. To effectively capture scale-dependent temporal dynamics, all experts adopt a unified lightweight structure termed the Local Representation Block (LRB). As illustrated in Fig. 2, the local feature extraction process is formulated as:

$$\mathbf{H}_i = \text{LRB}(\mathbf{X}_i) \in \mathbb{R}^{B \times C \times L_i}, \quad (5)$$

the LRB employs a streamlined pipeline comprising a standard 1D convolution, followed by a depthwise convolution for spatial-domain modeling and a pointwise convolution for cross-

channel feature fusion [44]. Batch normalization [45] and GELU activations [46] are integrated throughout the block, with a dropout layer applied after the final projection to prevent overfitting.

2) *Frequency-Domain Alignment*: As depicted in the final stage of Fig. 3, the multi-scale intermediate features extracted by the LRB must be aggregated. However, temporal resampling generates expert feature maps of varying lengths, making direct fusion infeasible. To enable coherent fusion, we align these intermediate features to a predefined target temporal length L_a in the frequency domain.

Specifically, for the i -th expert feature \mathbf{H}_i , we apply a real Fast Fourier Transform (FFT), perform a spectral length-matching operation $\mathcal{P}(\cdot, L_a)$, and reconstruct the aligned time-domain feature $\tilde{\mathbf{H}}_i$ via the inverse FFT. This alignment process is formulated as:

$$\begin{aligned} \mathbf{S}_i &= \mathcal{F}(\mathbf{H}_i) \in \mathbb{C}^{B \times C \times (\lfloor L_i/2 \rfloor + 1)}, \\ \tilde{\mathbf{S}}_i &= \mathcal{P}(\mathbf{S}_i, L_a) \in \mathbb{C}^{B \times C \times (\lfloor L_a/2 \rfloor + 1)}, \\ \tilde{\mathbf{H}}_i &= \mathcal{F}^{-1}(\tilde{\mathbf{S}}_i) \in \mathbb{R}^{B \times C \times L_a}. \end{aligned} \quad (6)$$

where $\mathcal{F}(\cdot)$ and $\mathcal{F}^{-1}(\cdot)$ denote the temporal real FFT and its inverse, respectively. Since the input features are real-valued, their spectrum exhibits conjugate symmetry. Consequently, \mathcal{F} retains only the $\lfloor L_i/2 \rfloor + 1$ non-negative frequency components. The operator \mathcal{P} then adjusts this spectrum to the target length by zero-padding the high-frequency components if $L_a > L_i$, and truncating them otherwise.

This frequency-domain alignment effectively preserves the dominant spectral structure of the extracted features under the

band-limited assumption, ensuring information integrity during the multi-scale fusion process.

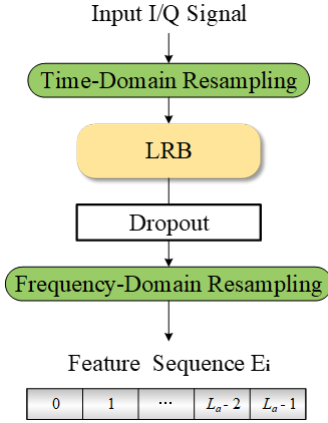


Fig. 3. Processing pipeline of the i -th expert branch, sequentially executing time-domain and frequency-domain resampling.

3) *Adaptive Gate Router and Feature Projection*: A limitation of static multi-scale fusion is that it assumes a uniform scale contribution across all inputs. This paradigm is suboptimal for AMR, as distinct modulation schemes and time-varying channel conditions dynamically rely on varying temporal resolutions. To address this, we introduce an input-dependent gating mechanism to adaptively allocate expert contributions.

As illustrated in the routing branch of Fig. 4, the gating network first processes the input sequence \mathbf{X} using a LRB, maintaining architectural consistency with the expert branches. The extracted feature map is then aggregated into a global routing vector via temporal pooling:

$$\mathbf{g} = \text{GAP}(\text{LRB}(\mathbf{X})) \in \mathbb{R}^{B \times C_g}, \quad (7)$$

where $\text{LRB}(\cdot)$ denotes the feature extraction mapped by the LRB, and $\text{GAP}(\cdot)$ applies global average pooling along the temporal dimension.

The normalized expert routing weights are subsequently generated via a multi-layer perceptron (MLP) coupled with a Softmax activation:

$$\boldsymbol{\alpha} = \text{Softmax}(\text{MLP}(\mathbf{g})) \in \mathbb{R}^{B \times N}, \quad (8)$$

ensuring that $\sum_{i=1}^N \alpha_{b,i} = 1$ for each instance b . In contrast to sparse MoE routing paradigms, we employ a dense soft gating mechanism. This configuration allows all experts to contribute simultaneously to the final representation, which is highly beneficial for AMR where informative structures at multiple temporal scales frequently coexist within a single signal.

The fused multi-scale representation is then computed as the α -weighted sum of the aligned expert features:

$$\mathbf{H}_{\text{MoE}} = \sum_{i=1}^N \alpha_i \tilde{\mathbf{H}}_i. \quad (9)$$

Finally, to prepare the aggregated features for subsequent global modeling, we apply a feature projection module:

$$\mathbf{F} = \mathcal{P}_{\text{proj}}(\mathbf{H}_{\text{MoE}}) \in \mathbb{R}^{B \times d_2 \times L_a}, \quad (10)$$

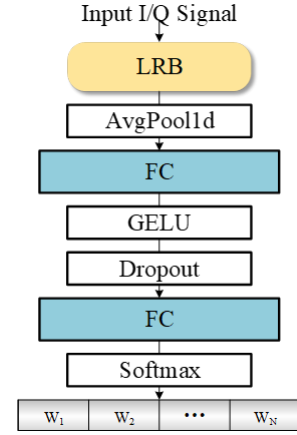


Fig. 4. Adaptive gating network for dynamic expert routing.

where $\mathcal{P}_{\text{proj}}(\cdot)$ denotes a composite projection mapping. Specifically, it comprises a DWConv1D with Batch Normalization, followed by a PWConv1D activated by GELU, and a final PWConv1D with Dropout. This module effectively refines the local contextual features, mitigates cross-scale redundancy introduced during fusion, and projects the channel dimension to match the Transformer encoder dimension d_2 .

B. Transformer-Based Global Temporal Modeling

While the MoE front-end effectively extracts scale-specific local features, AMR intrinsically requires modeling long-range temporal dependencies. Channel-induced temporal correlations, phase drifts, and symbol timing relationships cannot be comprehensively captured by localized convolutions. Therefore, we introduce a Transformer encoder stack to model these global temporal structures.

The projected sequence $\mathbf{F} \in \mathbb{R}^{B \times d_{\text{model}} \times L_a}$ is processed by a stack of L pre-normalized Transformer encoder blocks, where the embedding dimension d_{model} directly corresponds to the output channel size defined in the preceding feature projection module. Each block comprises a Multi-Head Self-Attention (MHSA) module enhanced with RoPE, followed by a Convolutional Feed-Forward Network (CFFN).

1) *Multi-Head Self-Attention with RoPE*: For the l -th encoder block, the layer-normalized input is first linearly projected into query (\mathbf{Q}), key (\mathbf{K}), and value (\mathbf{V}) representations, each with a channel dimension of $d_h = d_{\text{model}}$. These representations are uniformly divided into H attention heads, with a per-head dimension of $d_h = d_{\text{model}}/H$.

Standard absolute positional encoding is suboptimal for AMR, where relative temporal phase and timing relationships carry more physical significance than absolute sample indices. To inject relative positional inductive biases, we apply RoPE to the queries and keys. For a feature pair (x_{2k}, x_{2k+1}) at temporal position t , the rotary transformation is defined as:

$$\begin{pmatrix} x'_{2k} \\ x'_{2k+1} \end{pmatrix} = \begin{pmatrix} \cos \theta_t & -\sin \theta_t \\ \sin \theta_t & \cos \theta_t \end{pmatrix} \begin{pmatrix} x_{2k} \\ x_{2k+1} \end{pmatrix}. \quad (11)$$

Although this rotation is performed in the learned embedding space rather than the physical signal domain, it provides a

TABLE I
SUMMARY OF DATASET SPECIFICATIONS AND TRAINING HYPERPARAMETERS

	RadioML2016.10a	RadioML2016.10b	RadioML2018.01A
Modulation Types	BPSK, QPSK, 8PSK, 16QAM, 64QAM, GFSK, CPFSK, PAM4, AM-DSB, AM-SSB, WBFM	BPSK, QPSK, 8PSK, 16QAM, 64QAM, GFSK, CPFSK, PAM4, AM-DSB, WBFM	OOK, 4ASK, 8ASK, BPSK, QPSK, 8PSK, 16PSK, 32PSK, 16APSK, 32APSK, 64APSK, 128APSK, 16QAM, 32QAM, 64QAM, 128QAM, 256QAM, OQPSK, GMSK, AM-SSB-WC, AM-SSB-SC, AM-DSB-WC, AM-DSB-SC, FM
SNR Range	-20:2:18 dB	-20:2:18 dB	-20:2:30 dB
Sample Format	2×128	2×128	2×1024
Number of Samples	220,000	1,200,000	2,555,904
Dataset Partition	6:2:2	6:2:2	6:2:2
Batch Size	128	128	512
Loss Function	Cross-Entropy	Cross-Entropy	Cross-Entropy
Optimizer	AdamW	AdamW	AdamW
Learning Rate	0.001	0.001	0.001
LR Scheduler	ReduceLROnPlateau	ReduceLROnPlateau	ReduceLROnPlateau
Epochs	100	100	100
Early Patience	15	15	15

geometric inductive bias that aligns with the phase evolution characteristics of modulated signals.

Let $\tilde{\mathbf{Q}}$ and $\tilde{\mathbf{K}}$ denote the rotated queries and keys. The MHSA efficiently captures global dependencies via scaled dot-product attention. Incorporating the residual connection, the output of the attention module is formulated as:

$$\mathbf{Z}_l = \mathbf{F}_l + \text{MHSA}(\tilde{\mathbf{Q}}, \tilde{\mathbf{K}}, \mathbf{V}), \quad (12)$$

where $\text{MHSA}(\cdot)$ computes and concatenates the attention outputs across all H heads, followed by a linear projection.

2) *Convolutional Feed-Forward Network (CFFN)*: To complement the global attention mechanism with fine-grained local structural refinement, we replace the standard position-wise FFN with a Convolutional FFN. The complete forward pass for the remaining part of the l -th block is concisely given by:

$$\begin{aligned} \text{CFFN}(\mathbf{Z}_l) &= \mathcal{L}_2(\text{DWConv1D}(\sigma(\mathcal{L}_1(\mathbf{Z}_l)))) \\ \mathbf{F}_{l+1} &= \mathbf{Z}_l + \text{CFFN}(\text{LN}(\mathbf{Z}_l)), \end{aligned} \quad (13)$$

where $\text{LN}(\cdot)$ denotes Layer Normalization, \mathcal{L}_1 and \mathcal{L}_2 are pointwise linear layers for channel expansion and reduction, respectively, and σ represents the SiLU activation. This architectural modification explicitly reintroduces local sequence interactions, ensuring that both global contextual dependencies and local transitional features are robustly modeled before final classification.

C. Attention-Based Temporal Aggregation and Classification

The encoder output is still a temporal sequence, whereas the recognition target is sequence-level. Uniform aggregation may dilute informative temporal segments, especially when modulation cues are unevenly distributed or partially corrupted by noise. We therefore employ attention pooling to emphasize salient temporal regions.

Let $\{\mathbf{F}_t\}_{t=1}^{L_a}$ denote the encoder output sequence. The attention weight of the t -th time step is defined as

$$\beta_t = \frac{\exp(\mathbf{w}^\top \tanh(\mathbf{F}_t))}{\sum_{j=1}^{L_a} \exp(\mathbf{w}^\top \tanh(\mathbf{F}_j))}, \quad (14)$$

where \mathbf{w} is a learnable parameter vector. The global representation is then obtained by

$$\mathbf{z} = \sum_{t=1}^{L_a} \beta_t \mathbf{F}_t. \quad (15)$$

Compared with average pooling, this data-dependent aggregation strategy can suppress uninformative or noisy intervals while retaining discriminative temporal evidence. The aggregated representation \mathbf{z} is finally fed into a linear classifier to predict the posterior distribution over modulation categories.

IV. EXPERIMENTS AND RESULTS

A. Evaluation Datasets and Experimental Setup

We evaluate the proposed MoEformer on three widely used AMR benchmarks: RadioML2016.10a [13], RadioML2016.10b [18], and RadioML2018.01A [17]. These datasets represent progressively more challenging recognition scenarios, ranging from short I/Q sequences under synthetic impairments to large-scale long-sequence settings with substantially increased modulation diversity and channel distortions.

As summarized in Table I, RadioML2016.10a contains 11 modulation categories and covers an SNR range from -20 dB to 18 dB in steps of 2 dB. Each sample is represented as a 2×128 I/Q sequence, with 1,000 samples for each modulation-SNR pair. RadioML2016.10b follows the same input format and SNR range, but focuses on 10 modulation types, substantially increases the sample size and introduces stronger impairments such as multipath fading, carrier frequency offset, and sampling rate offset. In contrast, RadioML2018.01A is considerably larger and more complex, containing 24 modulation types

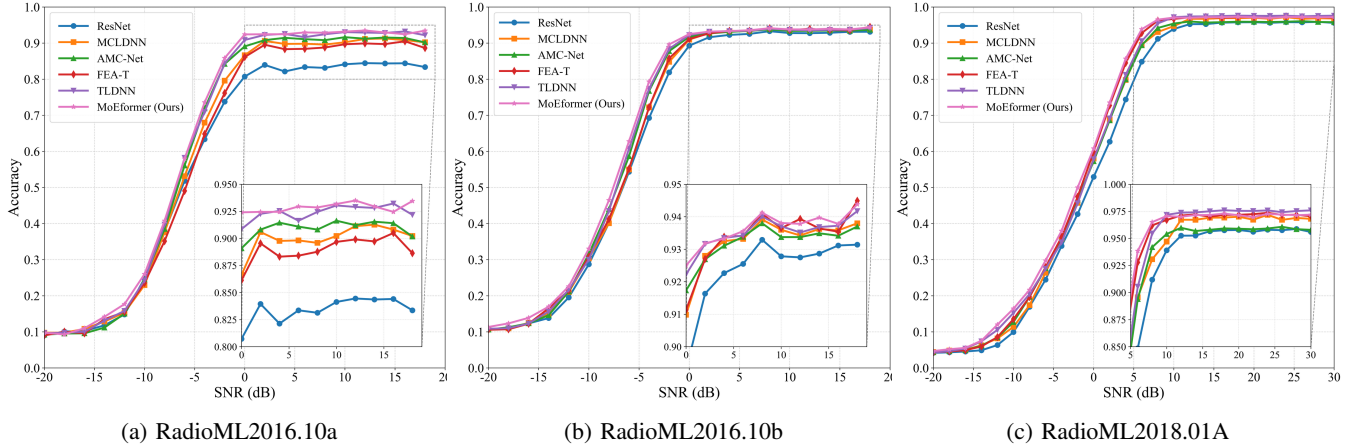


Fig. 5. Comparison of classification accuracy versus SNR across three benchmark datasets.

TABLE II
PERFORMANCE COMPARISON OF ALL METHODS ON THREE DATASETS

Model	RadioML2016.10a				RadioML2016.10b				RadioML2018.01A			
	Ave. Acc.	Max. Acc.	Params (K)	Latency (ms)	Ave. Acc.	Max. Acc.	Params (K)	Latency (ms)	Ave. Acc.	Max. Acc.	Params (K)	Latency (ms)
ResNet	57.08%	84.45%	96.30	0.0318	63.27%	93.29%	96.17	0.0143	60.32%	95.88%	164.18	0.0321
MCLDNN	60.99%	91.27%	406.20	0.0381	64.25%	93.92%	406.07	0.0278	62.23%	97.18%	407.88	0.1301
AMC-Net	61.96%	91.64%	466.14	0.0343	65.05%	93.80%	465.63	0.0337	62.10%	96.07%	2042.22	0.0472
FEA-T	59.80%	90.50%	168.59	0.0811	64.54%	94.49%	168.55	0.0802	63.37%	97.37%	171.86	0.0625
TLDNN	63.00%	93.23%	243.34	0.0405	65.33%	94.18%	243.31	0.0411	63.17%	97.60%	276.66	0.0445
MoEformer	63.74%	93.50%	187.73	0.0591	66.24%	94.38%	187.60	0.0595	64.22%	97.29%	237.27	0.0676

and more than 2.5 million samples, each with a sequence length of 2×1024 . Owing to its longer observation window, larger category set, and richer distortion patterns, this dataset is particularly suitable for evaluating long-range temporal modeling capability.

For all datasets, samples are split into training, validation, and test subsets with a fixed ratio of 6:2:2 within each modulation class and SNR level. Prior to training, all I/Q sequences were L2-normalized. All experiments are implemented in PyTorch and conducted on a single NVIDIA RTX 4090 GPU. Unless otherwise specified, the model is trained using cross-entropy loss and optimized by AdamW with an initial learning rate of 0.001 and a weight decay coefficient of 0.01. The learning rate is scheduled by ReduceLROnPlateau, where the learning rate is multiplied by 0.5 once the validation loss fails to improve for five consecutive epochs. The maximum number of training epochs is set to 100, and early stopping with a patience of 15 epochs is adopted to prevent overfitting. The batch size is set to 128 for RadioML2016.10a and RadioML2016.10b, and 512 for RadioML2018.01A.

B. Overall Performance Comparison

We compare MoEformer with five representative deep-learning-based AMR baselines, including ResNet [17], MCLDNN [26], AMC-Net [47], FEA-T [48], and TLDNN [49]. Among them, ResNet, MCLDNN, AMC-Net, and FEA-T take raw I/Q sequences as input, whereas TLDNN uses amplitude-phase representations transformed from the original

I/Q samples. Consequently, this selection of baselines ensures a comprehensive evaluation, benchmarking the proposed method against both standard raw I/Q-based architectures and models relying on alternative feature representations.

As reported in Table II, MoEformer consistently achieves the highest average classification accuracy across all three benchmark datasets. Specifically, on RadioML2016.10a, the model attains an average accuracy of 63.74%, outperforming the strongest baseline (TLDNN) by a margin of 0.74% and surpassing legacy architectures like ResNet by up to 6.66%. Similar performance trends are observed on RadioML2016.10b (66.24%) and the more challenging RadioML2018.01A (64.22%), where MoEformer retains its competitive edge. These results underscore the robustness of the proposed architecture across varying sequence lengths, dataset scales, and modulation diversities.

Fig. 5 illustrates the classification accuracy of all evaluated models across varying SNRs. In the extremely low-SNR region, especially below -10 dB, the performance gap among all methods is relatively limited, since severe noise heavily corrupts class-discriminative features. As the SNR increases, however, the advantage of MoEformer becomes increasingly evident. Its accuracy rises more steadily and remains in the top tier across a broad SNR range, indicating that the proposed model is more effective at exploiting recoverable modulation structure once informative patterns emerge.

The per-class SNR curves in Fig. 6 further demonstrate that recognition difficulty is highly class-dependent. On Ra-

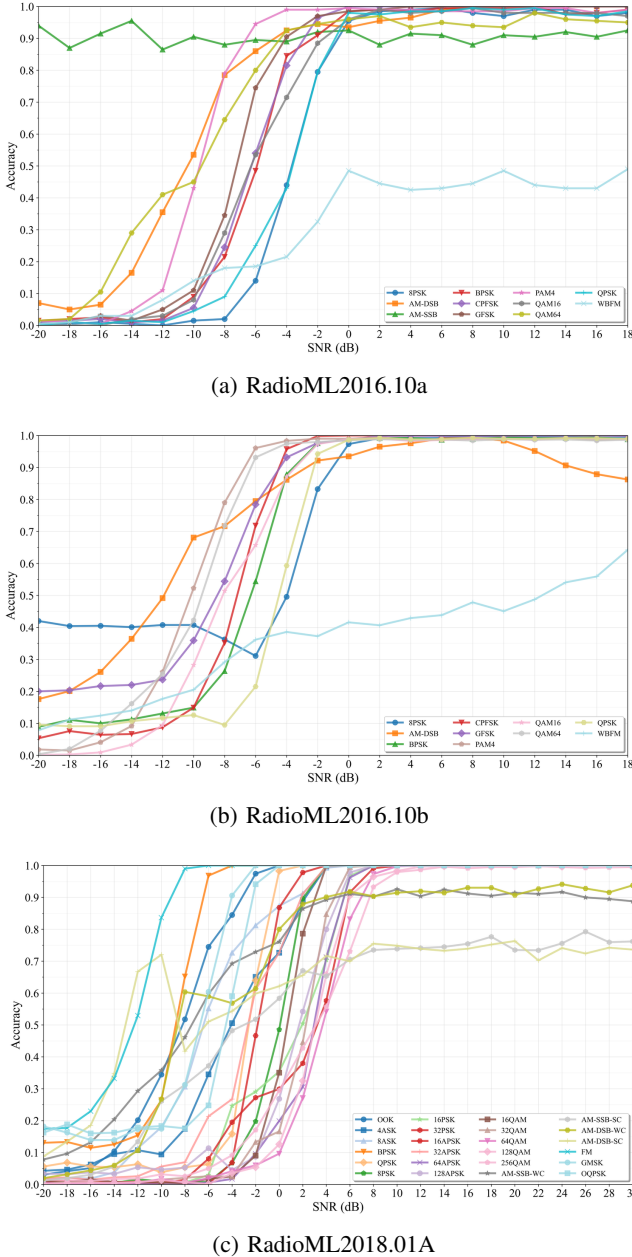


Fig. 6. Performance of different modulation schemes on three benchmark datasets.

RadioML2016.10a and RadioML2016.10b, analog schemes such as WBFM and AM-DSB remain relatively challenging. This difficulty inherently stems from the dataset generation process, where silent periods in the source audio cause these signals to temporarily degrade into indistinguishable unmodulated carriers. In contrast, most digital modulation schemes exhibit rapid accuracy convergence at SNRs above 0 dB. On RadioML2018.01A, confusions persist among neighboring high-order digital modulations, particularly between high-order QAM and adjacent PSK/APSCK categories. This confusion is physically attributed to their densely packed constellation diagrams, where the minimal Euclidean distance between adjacent symbol states increases susceptibility to boundary overlap caused by multipath fading and phase noise. These

observations delineate the performance boundaries imposed by the intrinsic physical structures and channel sensitivities of individual modulation formats.

As illustrated in Fig. 7, the confusion matrices provide a more fine-grained interpretation of the classification behavior under different SNR conditions. On the RadioML2016.10a and 2016.10b datasets, the predicted labels exhibit severe cross-classification between AM-DSB and WBFM. Notably, even at a high SNR of 12 dB, a substantial proportion of WBFM signals are persistently misclassified as AM-DSB, with the classification accuracy for WBFM remaining below 50%.

Regarding the RadioML2018.01A dataset, the matrices reveal that the error distribution is predominantly bounded within specific modulation families. At a low SNR of -6 dB, intra-family confusion is widespread. As the SNR increases to 12 dB, the proposed model achieves distinct separability for most phase and frequency modulations. The residual misclassifications are sharply localized, occurring primarily among the high-order digital formats, such as AM-DSB-WC and AM-DSB-SC. These matrix distributions visually confirm that while the network effectively mitigates noise-induced feature corruption, the ultimate classification bottlenecks align precisely with the fundamental signal ambiguities to the datasets.

C. Complexity and Efficiency Analysis

In addition to recognition accuracy, practical AMR systems must evaluate computational efficiency. We compare the baseline methods in terms of parameter count and inference latency, as detailed in Table II.

MoFormer demonstrates distinct parameter efficiency across all datasets. For RadioML2016.10a and RadioML2016.10b, the model utilizes approximately 187.73K parameters, maintaining a substantially smaller memory footprint than heavily parameterized baselines such as MCLDNN, AMC-Net, and TLDNN. On RadioML2018.01A, it requires 237.27K parameters, remaining more compact than AMC-Net and MCLDNN, and only moderately larger than FEA-T. This confirms that the observed performance improvements stem from the multi-scale feature extraction and adaptive expert routing mechanisms, rather than a brute-force expansion in model capacity.

However, this architectural sophistication introduces specific trade-offs. Computationally, the model records an inference latency of roughly 0.0591 ms on RadioML2016.10a/b and 0.0676 ms on RadioML2018.01A. While this remains within a practically acceptable range and is lower than that of the heavier models, it is higher than lightweight baselines like ResNet (0.0318 ms) and TLDNN (0.0405 ms). This increase is primarily attributed to the inherent overhead of dynamic gating and attention operations. Furthermore, a performance trade-off is observed regarding peak accuracy: although MoFormer secures the highest overall average accuracy, its peak accuracy is marginally surpassed by FEA-T on RadioML2016.10b and TLDNN on RadioML2018.01A. This implies that while the adaptive mechanism excels at mitigating severe signal distortions in low-SNR conditions, absolute peak performance in high-SNR scenarios presents minor room for refinement. Overall, MoFormer achieves a viable balance between predictive robustness and deployment efficiency.

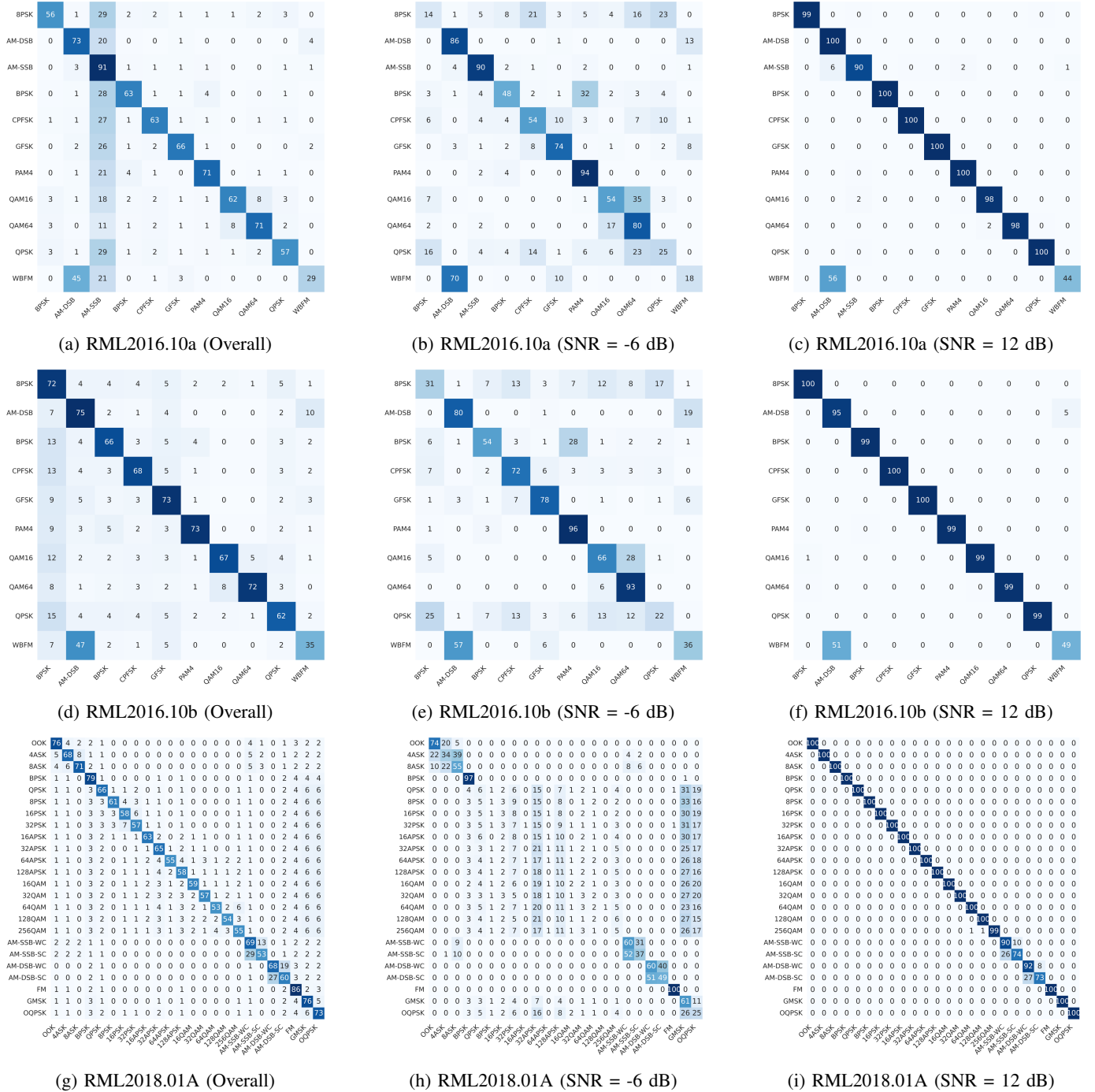


Fig. 7. Confusion matrices for modulation classification across three benchmark RadioML datasets under varying SNR conditions.

D. Visualization and Representation Analysis

As shown in Fig. 8, the t-SNE visualizations [50] of the learned feature representations obtained by the proposed method on the RadioML2016.10a, RadioML2016.10b, and RadioML2018.01A datasets at 0 dB and 12 dB SNR conditions are presented. At 0 dB, most modulation types in the RadioML2016 series datasets begin to form preliminary cluster structures; however, noticeable feature overlap can still be observed between several specific classes. For instance, AM-DSB and WBFM exhibit closely distributed features in the

embedding space, and a certain degree of overlap remains between QAM16 and QAM64, which can be attributed to the similarity of their constellation structures and statistical characteristics. This phenomenon is more pronounced on the RadioML2018.01A dataset, where low-order PSK modulations, high-order QAM modulations, as well as amplitude-modulated signals such as AM-DSB-WC and AM-SSB-WC, and AM-DSB-SC and AM-SSB-SC, exhibit relatively compact and overlapping distributions. As the SNR increases to 12 dB, the feature representations corresponding to different modulation types gradually converge into more compact and well-separated

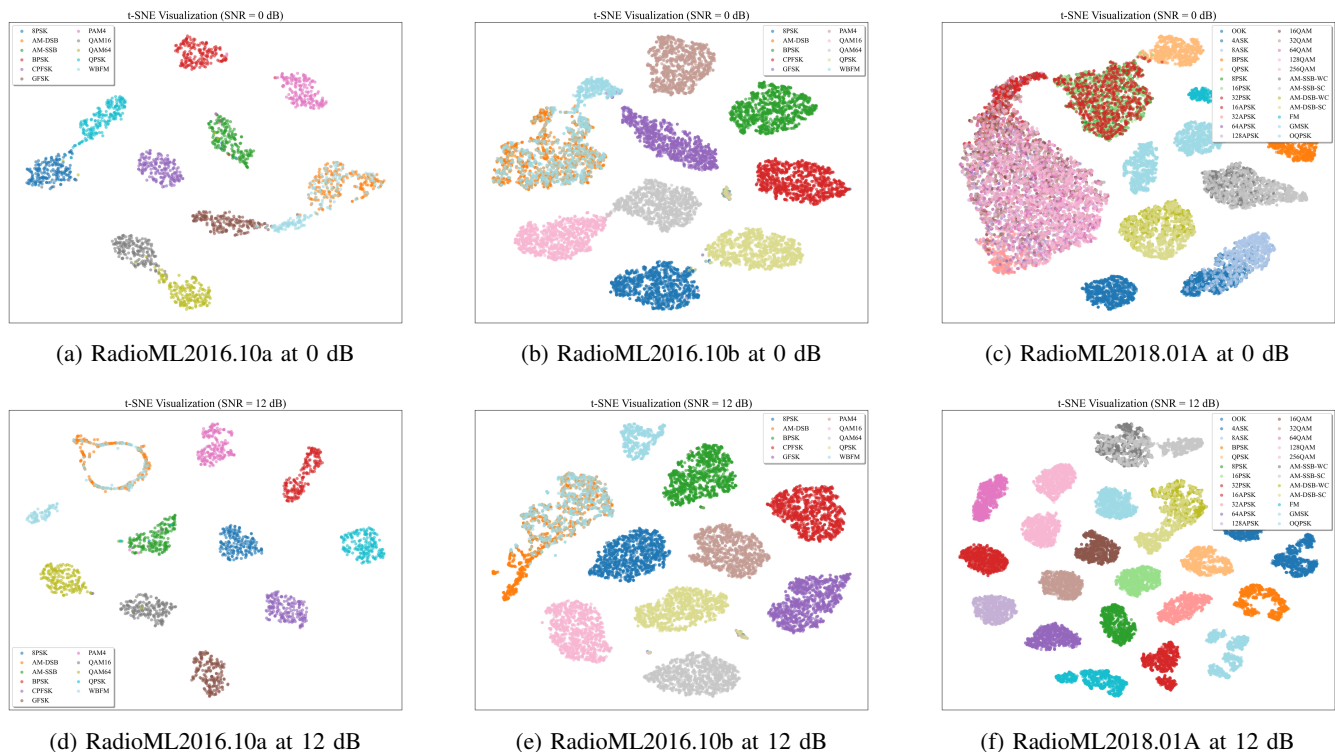


Fig. 8. t-SNE visualizations of learned modulation feature representations across three benchmark datasets at 0 dB and 12 dB SNR.

TABLE III
ABLATION STUDY ON MULTI-SCALE EXPERT CONFIGURATIONS WITH DIFFERENT TEMPORAL SCALE FACTORS.

Configuration	RadioML2016.10a			RadioML2016.10b			RadioML2018.01A		
	Avg. Acc. (%)	Params (K)	Latency (ms)	Avg. Acc. (%)	Params (K)	Latency (ms)	Avg. Acc. (%)	Params (K)	Latency (ms)
E1 [1.0]	61.72	183.31	0.0447	65.70	183.18	0.0457	61.95	221.95	0.0466
E2 [1.0, 2.0]	62.46	184.78	0.0500	65.52	184.65	0.0495	62.26	227.06	0.0536
E3 [0.5, 1.0, 2.0]	61.72	186.26	0.0549	65.87	186.13	0.0543	62.52	232.16	0.0592
E4 [0.5, 0.75, 1.0, 2.0]	62.02	187.73	0.0600	66.24	187.60	0.0595	62.60	237.27	0.0655
E4 [0.5, 1.0, 1.25, 2.0]	62.25	187.73	0.0599	65.93	187.60	0.0597	62.72	237.27	0.0655
E4 [0.5, 1.0, 1.5, 2.0]	63.74	187.73	0.0591	65.88	187.60	0.0589	64.22	237.27	0.0676
E5 [0.5, 0.75, 1.0, 1.5, 2.0]	61.91	189.20	0.0649	65.61	189.07	0.0650	62.67	242.37	0.0719

clusters, with the overlap between QAM16 and QAM64 and among different orders of PSK modulations being significantly alleviated. Nevertheless, in scenarios involving a large number of modulation types with high inter-class similarity, a small amount of local overlap among amplitude-modulated signals can still be observed.

E. Ablation Studies

To verify that the performance gains of MoEformer arise from the proposed architectural components rather than incidental design choices, systematic ablation studies are conducted on the multi-scale expert configuration, pooling strategy, and positional encoding method.

1) *Impact of Multi-Scale Expert Configuration*: Table III details the impact of varying the number of experts and their temporal scale factors. Transitioning from a single-expert baseline (E1) to a multi-expert architecture consistently

improves performance, demonstrating the necessity of multi-resolution temporal modeling. A fixed temporal scale proves insufficient, as discriminative signal patterns inherently manifest at varying granularities depending on the specific modulation family and prevailing channel conditions.

Furthermore, the optimal scale combination exhibits dataset-specific sensitivities. The configuration of [0.5, 1.0, 1.5, 2.0] yields the highest average accuracy on RadioML2016.10a and RadioML2018.01A, whereas [0.5, 0.75, 1.0, 2.0] is superior on RadioML2016.10b. This divergence implies that datasets with distinct channel impairment profiles benefit from tailored, finer-grained temporal decomposition. Importantly, scaling the number of experts does not yield monotonic improvements. Extending the architecture to five experts degrades accuracy across all three datasets. This indicates that excessive expert diversity introduces feature redundancy and complicates the routing mechanism, ultimately hindering optimal decision-

TABLE IV
COMPARISON BETWEEN AVERAGE POOLING AND ATTENTION-BASED POOLING ON BENCHMARK DATASETS.

Dataset	Pooling	Avg. Acc. (%)	Params (K)	Latency (ms)
RadioML2016.10a	Average	63.14	187.47	0.0569
	Attention	63.74	187.73	0.0591
RadioML2016.10b	Average	65.86	187.47	0.0600
	Attention	66.24	187.60	0.0595
RadioML2018.01A	Average	62.79	237.14	0.0612
	Attention	64.22	237.27	0.0676

making.

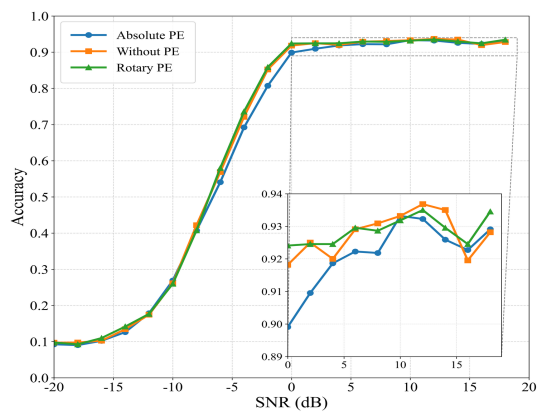
From an efficiency standpoint, while the parameter overhead of additional experts remains marginal, the corresponding latency increase is more pronounced. Consequently, the selected four-expert configuration establishes an optimal trade-off between classification accuracy and computational complexity.

2) *Effect of Pooling Strategy*: To evaluate the contribution of the pooling mechanism, attention-based pooling is compared with conventional average pooling, maintaining all other architectural components identical to the optimal configuration. As detailed in Table IV, the attention-based strategy consistently surpasses average pooling across all benchmark datasets, yielding absolute accuracy improvements of 0.6%, 0.38%, and 1.43% percentage points on RadioML2016.10a, RadioML2016.10b, and RadioML2018.01A, respectively. The more pronounced performance gain observed on RadioML2018.01A indicates that selective feature aggregation becomes increasingly critical for processing longer input sequences.

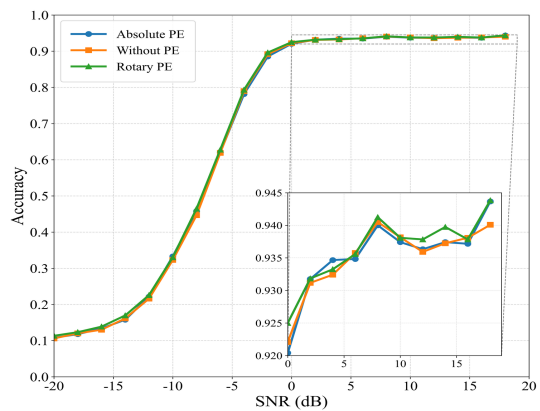
Average pooling assumes equal contributions of all feature channels to the final feature representation. Different from average pooling, attention-based pooling calculates adaptive channel weights to improve feature representation flexibility. This method dynamically enhances discriminative feature channels and suppresses invalid or less informative ones. Complexity evaluation results verify that this adaptive aggregation strategy only slightly increases network parameters. Although weight calculation slightly increases inference latency, the method achieves consistent classification performance gains with this trivial computational overhead.

3) *Effect of Positional Encoding*: We further compare three positional encoding strategies: RoPE, absolute positional encoding, and no positional encoding. As illustrated in Fig. 9, the performance variations exhibit distinct characteristics depending on the dataset scale. On RadioML2016.10a and RadioML2016.10b, the configuration without PE and the one utilizing RoPE display highly competitive trajectories, with both consistently surpassing absolute PE in the medium-to-high SNR regimes. Conversely, on the larger and longer-sequence RadioML2018.01A dataset, RoPE achieves a pronounced and continuous performance gain over both absolute PE and the no-PE baseline across the entire SNR spectrum.

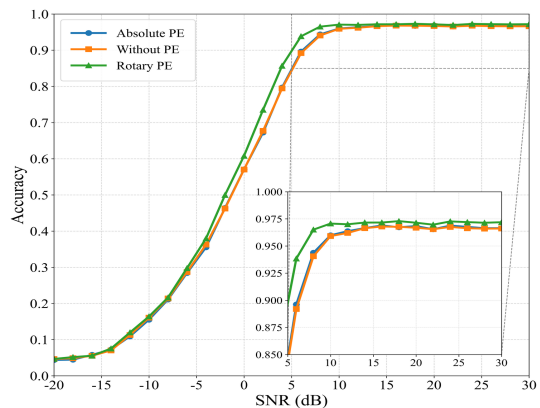
This divergence underscores the inherent mathematical limitations of absolute coordinates versus relative transformations in time-series modeling. Absolute PE binds fixed positional features to specific temporal indices, which can introduce



(a) RadioML2016.10a



(b) RadioML2016.10b



(c) RadioML2018.01A

Fig. 9. Performance comparison of different positional encoding strategies across benchmark datasets.

rigid structural constraints and potentially induce overfitting, particularly in shorter sequences where local patterns dominate. In contrast, RoPE provides a more flexible and effective inductive bias by explicitly encoding the relative distance between token pairs through coordinate rotation. This mathematical formulation inherently preserves shift invariance and effectively models decaying dependencies over extended contexts. Consequently, RoPE successfully captures the continuous structural trajectories within long I/Q sequences while avoiding the performance degradation associated with rigid absolute position

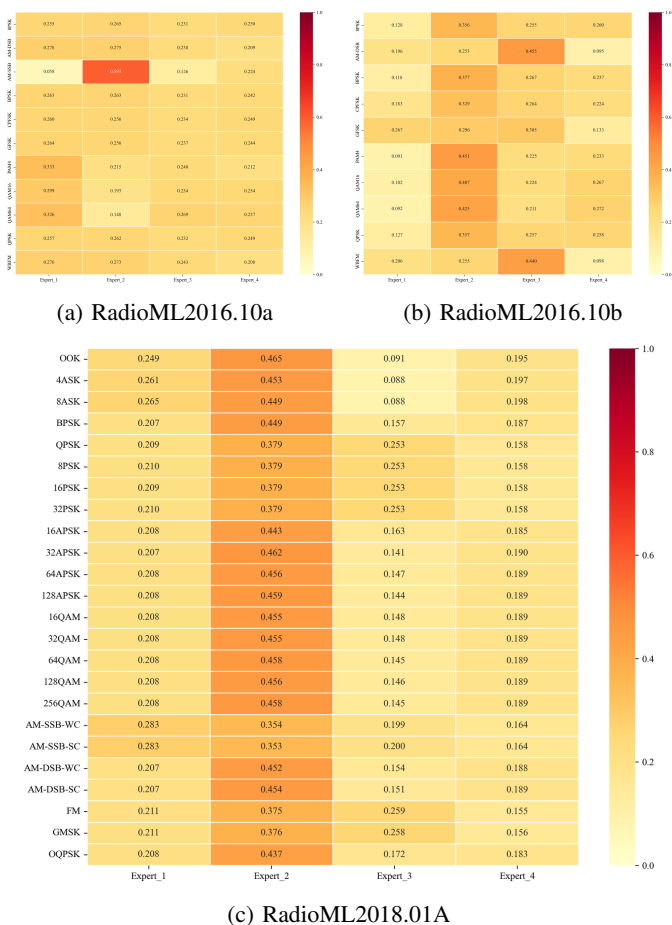


Fig. 10. Distribution of gating weights across modulation types on the RadioML datasets.

boundaries.

F. Additional Mechanism Analysis: Interpretability Analysis of the Gating Network

To evaluate the routing characteristics of the proposed MoE architecture, we analyze the statistical distribution of the gating network weights across various modulation types in Fig. 10. Experimental results reveal that rather than assigning weights randomly, the gating network adaptively learns highly structured and physically meaningful routing strategies based on the feature distributions of different datasets.

On the RadioML2016.10a dataset, the gating weights generally exhibit a relatively uniform load-balancing state. However, the model demonstrates local activation for specific, hard-to-distinguish modulation types. For instance, Expert 2 is assigned a dominant routing weight (0.593) when processing AM-SSB signals, indicating that under relatively simple data distributions, the MoE tends to isolate specific challenging tasks to a single expert.

On the RadioML2016.10b dataset, the routing mechanism performs a clear modular division based on the intrinsic physical properties of the signals. Expert 2 obtains the highest weights for digital modulations (particularly high-order schemes like PAM4, QAM16, and QAM64), whereas Expert

3 concentrates its computational resources on continuous-wave analog modulations, such as AM-DSB and WBFM. This divergence demonstrates the capability of the gating network to autonomously capture the fundamental differences in the feature space between digital and analog signals without relying on manual priors.

For the RadioML2018.01A dataset, Expert 2 functions as the primary expert, maintaining high and stable baseline weights across most modulation types to extract shared universal radio frequency features. Concurrently, other experts act as auxiliary experts to dynamically compensate for specific physical characteristics. Specifically, the weight of Expert 3 significantly increases to approximately 0.25 when processing phase- and frequency-sensitive modulations, while the weight of Expert 1 exhibits a noticeable increase for amplitude modulations.

V. CONCLUSION

In this paper, we proposed MoEformer, an adaptive multi-scale mixture-of-experts Transformer framework for automatic modulation recognition. Extensive experiments on three benchmark datasets showed that the proposed model outperforms representative deep learning baselines and achieves a favorable trade-off between recognition accuracy and model complexity. The results suggest that input-adaptive multi-scale feature fusion is more effective than fixed fusion strategies for handling diverse modulation patterns under varying channel conditions, especially in complex scenarios and challenging SNR regimes. These findings confirm the value of adaptive temporal modeling for robust AMR. Future work will focus on more efficient expert routing and lightweight model designs for edge deployment.

REFERENCES

- [1] F. Restuccia and T. Melodia, "Deep learning at the physical layer: System challenges and applications to 5g and beyond," *IEEE Communications Magazine*, vol. 58, no. 10, pp. 58–64, 2020.
- [2] Y. A. Eldemerdash, O. A. Dobre, and M. Öner, "Signal identification for multiple-antenna wireless systems: Achievements and challenges," *IEEE Commun. Surveys Tuts.*, vol. 18, no. 3, pp. 1524–1551, 2016.
- [3] F. A. Bhatti, M. J. Khan, and A. Selim, "Shared spectrum monitoring using deep learning," *IEEE Trans. Cogn. Commun. Netw.*, vol. 7, no. 4, pp. 1172–1185, 2021.
- [4] M. Kulin, T. Kazaz, I. Moerman, and E. De Poorter, "End-to-end learning from spectrum data: A deep learning approach for wireless signal identification in spectrum monitoring applications," *IEEE Access*, vol. 6, pp. 18 484–18 501, 2018.
- [5] O. A. Dobre, A. Abdi, Y. Bar-Ness, and W. Su, "Survey of automatic modulation classification techniques: Classical approaches and new trends," *IET Commun.*, vol. 1, no. 2, pp. 137–156, 2007.
- [6] V. G. Chavali and C. R. Da Silva, "Maximum-likelihood classification of digital amplitude-phase modulated signals in flat fading non-Gaussian channels," *IEEE Trans. Commun.*, vol. 59, no. 8, pp. 2051–2056, Aug. 2011.
- [7] A. K. Nandi and E. E. Azzouz, "Algorithms for automatic modulation recognition of communication signals," *IEEE Trans. Commun.*, vol. 46, no. 4, pp. 431–436, Apr. 1998.
- [8] L. Zhou, Z. Sun, and W. Wang, "Learning to short-time Fourier transform in spectrum sensing," *Phys. Commun.*, vol. 25, pp. 420–425, 2017.
- [9] M. Zhang, Y. Zeng, Z. Han, and Y. Gong, "Automatic modulation recognition using deep learning architectures," in *Proc. IEEE 19th Int. Workshop Signal Process. Adv. Wireless Commun. (SPAWC)*, 2018, pp. 1–5.
- [10] C. Park, J. Choi, S. Nah, W. Jang, and D. Y. Kim, "Automatic modulation recognition of digital signals using wavelet features and SVM," in *Proc. 10th Int. Conf. Adv. Commun. Technol.*, 2008, pp. 387–390.

- [11] S. Peng, S. Sun, and Y.-D. Yao, "A survey of modulation classification using deep learning: Signal representation and data preprocessing," *IEEE Trans. Neural Netw. Learn. Syst.*, vol. 33, no. 12, pp. 7020–7038, Dec. 2022.
- [12] T. O'Shea and J. Hoydis, "An introduction to deep learning for the physical layer," *IEEE Trans. Cogn. Commun. Netw.*, vol. 3, no. 4, pp. 563–575, Dec. 2017.
- [13] T. J. O'Shea and N. West, "Radio machine learning dataset generation with GNU radio," in *Proc. GNU Radio Conf.*, 2016, pp. 1–6.
- [14] K. He, X. Zhang, S. Ren, and J. Sun, "Deep residual learning for image recognition," in *Proc. IEEE Conf. Comput. Vis. Pattern Recognit. (CVPR)*, Las Vegas, NV, USA, 2016, pp. 770–778.
- [15] N. E. West and T. J. O'Shea, "Deep architectures for modulation recognition," in *Proc. IEEE Int. Symp. Dyn. Spectr. Access Netw. (DySPAN)*, Baltimore, MD, USA, 2017, pp. 1–6.
- [16] F. Meng, P. Chen, L. Wu, and X. Wang, "Automatic modulation classification: A deep learning enabled approach," *IEEE Trans. Veh. Technol.*, vol. 67, no. 11, pp. 10760–10772, Nov. 2018.
- [17] T. J. O'Shea, T. Roy, and T. C. Clancy, "Over-the-air deep learning based radio signal classification," *IEEE J. Sel. Topics Signal Process.*, vol. 12, no. 1, pp. 168–179, Feb. 2018.
- [18] T. J. O'Shea, J. Corgan, and T. C. Clancy, "Convolutional radio modulation recognition networks," in *Proc. Eng. Appl. Neural Netw. (EANN)*, Aberdeen, U.K., 2016, pp. 213–226.
- [19] Y. Wang, M. Liu, J. Yang, and G. Gui, "Data-driven deep learning for automatic modulation recognition in cognitive radios," *IEEE Transactions on Vehicular Technology*, vol. 68, no. 4, pp. 4074–4077, 2019.
- [20] A. Krizhevsky, I. Sutskever, and G. E. Hinton, "ImageNet classification with deep convolutional neural networks," in *Proc. Adv. Neural Inf. Process. Syst. (NeurIPS)*, 2012, pp. 1097–1105.
- [21] C. Szegedy et al., "Going deeper with convolutions," in *Proc. IEEE Conf. Comput. Vis. Pattern Recognit. (CVPR)*, 2015, pp. 1–9.
- [22] S. Peng et al., "Modulation classification based on signal constellation diagrams and deep learning," *IEEE Trans. Neural Netw. Learn. Syst.*, vol. 30, no. 3, pp. 718–727, Mar. 2019.
- [23] S. Lin, Y. Zeng, and Y. Gong, "Modulation recognition using signal enhancement and multistage attention mechanism," *IEEE Trans. Wireless Commun.*, vol. 21, no. 11, pp. 9921–9935, Nov. 2022.
- [24] T. Chen, S. Zheng, K. Qiu, L. Zhang, Q. Xuan, and X. Yang, "Augmenting radio signals with wavelet transform for deep learning-based modulation recognition," *IEEE Trans. Cogn. Commun. Netw.*, vol. 10, no. 6, pp. 2029–2044, Dec. 2024.
- [25] W. Luo, Y. Li, R. Urtasun, and R. Zemel, "Understanding the effective receptive field in deep convolutional neural networks," in *Proceedings of the 30th International Conference on Neural Information Processing Systems (NIPS)*, Barcelona, Spain, 2016, pp. 4905–4913.
- [26] J. Xu, C. Luo, G. Parr, and Y. Luo, "A spatio temporal multi-channel learning framework for automatic modulation recognition," in *Proc. IEEE Wireless Commun. Lett.*, vol. 9, no. 10, Oct. 2020, pp. 1629–1632.
- [27] D. Hong, Z. Zhang, and X. Xu, "Automatic modulation classification using recurrent neural networks," in *Proc. IEEE Int. Conf. Comput. Commun. (ICCC)*, 2017, pp. 695–700.
- [28] S. Rajendran, W. Meert, D. Giustiniano, V. Lenders, and S. Pollin, "Deep learning models for wireless signal classification with distributed low-cost spectrum sensors," *IEEE Trans. Cogn. Commun. Netw.*, vol. 4, no. 3, pp. 433–445, Sep. 2018.
- [29] C. Z. et al., "A comprehensive survey on pretrained foundation models: A history from bert to chatgpt," 2023, arXiv:2302.09419.
- [30] Y. S. Chuang, C. L. Liu, and H. Y. Lee, "SpeechBERT: Cross-modal pre-trained language model for end-to-end spoken question answering," in *Proc. Interspeech*, 2020, pp. 4168–4172.
- [31] A. Dosovitskiy et al., "An image is worth 16x16 words: Transformers for image recognition at scale," in *Proc. Int. Conf. Learn. Represent. (ICLR)*, 2021, pp. 1–22.
- [32] A. Vaswani et al., "Attention is all you need," in *Proc. Adv. Neural Inf. Process. Syst. (NeurIPS)*, 2017, pp. 6000–6010.
- [33] Z. Zhang, C. Wang, C. Gan, S. Sun, and M. Wang, "Automatic modulation classification using convolutional neural network with features fusion of SPWVD and BJD," *IEEE Trans. Signal Inf. Process. Netw.*, vol. 5, no. 3, pp. 469–478, Sep. 2019.
- [34] X. Wang, D. Liu, Y. Zhang, Y. Li, and S. Wu, "A spatiotemporal multi-stream learning framework based on attention mechanism for automatic modulation recognition," *Digital Signal Process.*, vol. 130, p. 103703, 2022.
- [35] S. Ansari, S. Mahmoud, S. Majzoub, E. Almajali, A. Jarndal, and T. Bonny, "A novel lstm architecture for automatic modulation recognition: Comparative analysis with conventional machine learning and rnn-based approaches," *IEEE Access*, vol. 13, pp. 72 526–72 543, 2025.
- [36] S. Hamidi-Rad and S. Jain, "MCformer: A transformer based deep neural network for automatic modulation classification," in *Proc. IEEE Global Commun. Conf. (GLOBECOM)*, Madrid, Spain, 2021, pp. 1–6.
- [37] J. Zhang, S. An, F. Meng, and Q. Liu, "MST: A multi-scale transformer framework with cross-scale token fusion for automatic modulation recognition," *IEEE Wireless Communications Letters*, vol. 14, no. 12, pp. 4112–4116, 2025.
- [38] Z. Zhang, H. Luo, C. Wang, C. Gan, and Y. Xiang, "Automatic modulation classification using CNN-LSTM based dual-stream structure," *IEEE Transactions on Vehicular Technology*, vol. 69, no. 11, pp. 13 521–13 531, 2020.
- [39] W. Fedus, B. Zoph, and N. Shazeer, "Switch transformers: Scaling to trillion parameter models with simple and efficient sparsity," *J. Mach. Learn. Res.*, vol. 23, no. 120, pp. 1–39, 2022.
- [40] S. Mu and S. Lin, "A comprehensive survey of mixture-of-experts: Algorithms, theory, and applications," *arXiv preprint arXiv:2503.07137*, 2026.
- [41] W. Cai, J. Jiang, F. Wang, J. Tang, S. Kim, and J. Huang, "A survey on mixture of experts in large language models," *IEEE Transactions on Knowledge and Data Engineering*, pp. 1–20, 2025.
- [42] N. Shazeer, A. Mirhoseini, K. Maziarz, A. Davis, Q. Le, G. Hinton, and J. Dean, "Outrageously large neural networks: The sparsely-gated mixture-of-experts layer," in *Proc. Int. Conf. Learn. Represent. (ICLR)*, Toulon, France, 2017.
- [43] J. Su, Y. Lu, S. Pan, A. Murtadha, B. Wen, and Y. Liu, "Roformer: Enhanced transformer with rotary position embedding," *arXiv preprint*, vol. arXiv:2104.09864, 2021.
- [44] F. Chollet, "Xception: Deep learning with depthwise separable convolutions," in *Proc. IEEE Conf. Comput. Vis. Pattern Recognit. (CVPR)*, Honolulu, HI, USA, 2017, pp. 1251–1258.
- [45] S. Ioffe and C. Szegedy, "Batch normalization: Accelerating deep network training by reducing internal covariate shift," in *Proc. Int. Conf. Mach. Learn. (ICML)*, Lille, France, 2015, pp. 448–456.
- [46] D. Hendrycks and K. Gimpel, "Gaussian error linear units (gelus)," *arXiv preprint*, vol. arXiv:1606.08415, 2016.
- [47] J. Zhang, T. Wang, Z. Feng, and S. Yang, "AMC-Net: An effective network for automatic modulation classification," in *Proc. IEEE Int. Conf. Acoust., Speech Signal Process. (ICASSP)*, 2023, pp. 1–5.
- [48] Y. Chen, B. Dong, C. Liu, W. Xiong, and S. Li, "Abandon locality: Frame-wise embedding aided transformer for automatic modulation recognition," *IEEE Commun. Lett.*, vol. 27, no. 1, pp. 327–331, Jan. 2023.
- [49] Y. Qu, Z. Lu, R. Zeng, J. Wang, and J. Wang, "Enhancing automatic modulation recognition through robust global feature extraction," *arXiv preprint*, vol. arXiv:2401.01056, 2024.
- [50] L. van der Maaten and G. Hinton, "Visualizing data using t-sne," *J. Mach. Learn. Res.*, vol. 9, no. 86, pp. 2579–2605, 2008.